Iron-Doped Nickel Oxide Nanocrystals as Highly Efficient Electrocatalysts for Alkaline Water Splitting

Ksenia Fominykh,[†] Petko Chernev,[‡] Ivelina Zaharieva,[‡] Johannes Sicklinger,[†] Goran Stefanic,[§] Markus Döblinger,[†] Alexander Müller,[∥] Aneil Pokharel,[†] Sebastian Böcklein,[†] Christina Scheu,[∥] Thomas Bein,[*,†] and Dina Fattakhova-Rohlfing[*,†]

[†]University of Munich (LMU) and Center for NanoScience (CeNS), Butenandtstrasse 5-13 (E), 81377 Munich, Germany, [‡]Freie Universität Berlin, Arnimallee 14, 14195 Berlin, Germany, [§]Division of Materials Chemistry, Ruđer Bošković Institute, P.O. Box 180, HR-10002 Zagreb, Croatia, and [∥]Max-Planck-Institut für Eisenforschung, Max-Planck-Straße 1, 40237 Düsseldorf, Germany

ABSTRACT Efficient electrochemical water splitting to hydrogen and oxygen is considered a promising technology to overcome our dependency on fossil fuels. Searching for novel catalytic materials for electrochemical oxygen generation is essential for improving the total efficiency of water splitting processes. We report the synthesis, structural characterization, and electrochemical performance in the oxygen evolution reaction of Fe-doped NiO nanocrystals. The facile solvothermal synthesis in *tert*-butanol leads to the formation of ultrasmall crystalline and highly dispersible $Fe_xNi_{1-x}O$ nanoparticles with dopant concentrations of up to 20%. The increase in Fe content is accompanied by a decrease in particle size, resulting in nonagglomerated nanocrystals of 1.5−3.8 nm in size. The Fe content and composition of the nanoparticles are determined by X-ray photoelectron spectroscopy and energy-dispersive X-ray spectroscopy measurements, while Mössbauer and extended X-ray absorption fine structure analyses reveal a substitutional incorporation of Fe(III) into the NiO rock salt structure. The excellent dispersibility of the nanoparticles in ethanol allows for the preparation of homogeneous *ca.* 8 nm thin films with a smooth surface on various substrates. The turnover frequencies (TOF) of these films could be precisely calculated using a quartz crystal microbalance. $Fe_{0.1}Ni_{0.9}O$ was found to have the highest electrocatalytic water oxidation activity in basic media with a TOF of 1.9 s^{-1} at the overpotential of 300 mV. The current density of 10 mA cm^{-2} is reached at an overpotential of 297 mV with a Tafel slope of 37 mV dec^{-1}. The extremely high catalytic activity, facile preparation, and low cost of the single crystalline $Fe_xNi_{1-x}O$ nanoparticles make them very promising catalysts for the oxygen evolution reaction.

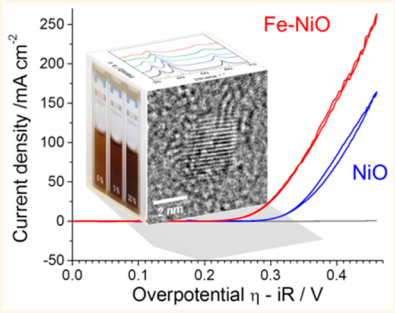

KEYWORDS: iron-doped nickel oxide · nanoparticles · electrocatalysis · oxygen evolution · water splitting

The splitting of water into oxygen and hydrogen provides a promising solution to the generation and storage of hydrogen from renewable energy sources, such as solar and wind power.[1,2] For high-rate hydrogen production both half-reactions of the water splitting process, *i.e.*, water oxidation and reduction, have to proceed with optimum efficiency. The hydrogen evolution reaction follows a simple mechanism and can be catalyzed by many metals and metal oxides at low overpotentials.[3] A major challenge however is the slow rate of the oxygen evolution reaction (OER), which proceeds *via* several steps with high activation energies requiring large overpotentials for the transfer of four electrons.[4,5] To solve this problem, efficient water oxidation catalysts are needed, which has initiated an intensive search on different classes of materials acting as possible OER catalysts.[6−15] The state of the art electrocatalysts for oxygen generation are expensive and rare iridium and ruthenium oxides,[1,2,16−18] severely restricting their large-scale applications. More attractive alternatives such as abundant and low-cost first-row transition metal oxides have been intensively explored as OER catalysts, but their long-term stability and catalytic performance were found to be inferior.[18] Recent developments, however, demonstrate that the OER activity of these materials can be substantially enhanced and tuned in a broad range by substitutional doping with different ions, resulting in mixed compounds such as $Ni_{1-x}Fe_xO$

* Address correspondence to dina.fattakhova@cup.lmu.de, bein@lmu.de.

Received for review January 23, 2015 and accepted April 1, 2015.

Published online April 01, 2015
10.1021/acsnano.5b00520

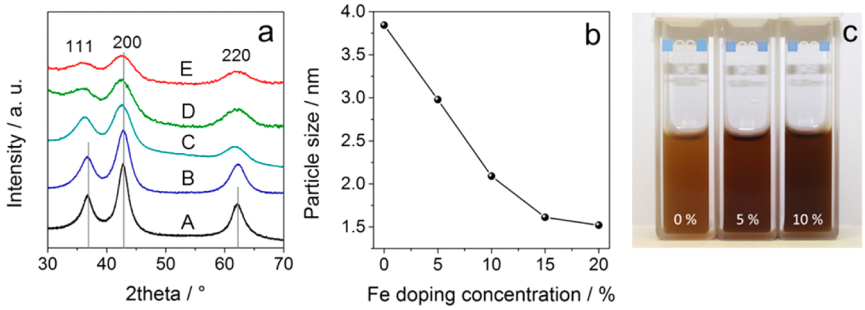

Figure 1. Crystallite size and dispersions of the $Fe_xNi_{1-x}O$ nanoparticles with different Fe doping concentration: (a) Powder XRD patterns of the dried $Fe_xNi_{1-x}O$ nanoparticles NP-0% (A), NP-5% (B), NP-10% (C), NP-15% (D), and NP-20% (E) (NiO pattern: ICDD card number 01-071-1179). (b) Crystalline domain size of nanoparticles with increasing Fe content calculated from the XRD patterns using the Scherrer equation for the most intensive (200) NiO signal at $2\theta = 43°$. (c) Image of $Fe_xNi_{1-x}O$ nanoparticle dispersions (concentration: 2 mg mL^{-1}) in ethanol; the numbers indicate the Fe doping concentrations.

with very high catalytic activities at low overpotentials comparable to that of IrO_2.[19−21]

Fe−Ni−O mixed compounds have been known for decades and are considered among the best electrocatalysts for alkaline water electrolysis.[22−26] Still, the numerous publications reported up to date demonstrate the very strong impact of crystalline structure and morphology on the electrocatalytic activity, which can differ by orders of magnitude for different Fe−Ni−O compounds.[19,21,27,28] Most of the literature on the subject concerns layered structures such as Ni−Fe double hydroxides (Fe/Ni$(OH)_2$),[27,29] oxyhydroxides (Fe/NiOOH),[19] or amorphous phases[30,31] either formed directly or as a result of structural transformations of NiO_x.[13] The activity of rock salt-type nickel oxide compounds was considered to be inferior due to their compact structure resulting in a low accessibility of catalytically active sites. We have recently demonstrated that the catalytic performance of rock salt-type nickel oxide increases dramatically due to a decrease in the particle size.[32] In the present work we demonstrate that the electrocatalytic activity increases by almost an order of magnitude by introducing Fe atoms into the structure, which makes it by far the highest among all reported FeNi oxide materials and, indeed, to our knowledge among all reported alkaline OER catalysts.[13,19−21]

We present for the first time a solvothermal synthesis pathway for the preparation of ultrasmall, crystalline, and dispersible Fe-doped NiO nanoparticles (NPs) with Fe contents of up to 20 mol % using *tert*-butanol (*t*BuOH) as solvent and reactant, as well as their application as highly efficient electrocatalyst for the oxygen evolution reaction. The particles show the highest turnover frequency (TOF) of 1.9 s^{-1} at an overpotential of 300 mV for 10% Fe(III)-doping, thus outperforming bulk iron nickel oxide and expensive rare earth iridium oxide catalysts. The combination of decreased particle size and high crystallinity is highly beneficial for the greatly enhanced electrocatalytic activity and the stability of the structure, which remains preserved after prolonged electrolysis in basic media. The material contains inexpensive, abundant elements and meets the criteria of high catalytic activity at low overpotentials, stability in basic media, and low cost, making this OER catalyst environmentally and economically attractive.

RESULTS AND DISCUSSION

For the synthesis of crystalline NiO nanoparticles doped with Fe(III) we used a solvothermal reaction in *tert*-butanol that leads to the direct formation of crystalline nanoparticles *via* a chemical reaction with the solvent. The suitability of this reaction pathway for the fabrication of ultrasmall colloidal nanocrystals was demonstrated by us in previous reports for several titanate systems and undoped NiO nanoparticles.[32−35] Key to the successful fabrication of doped and mixed oxides without phase separation is matching the reactivity of Fe and Ni precursors. Nickel(II) acetylacetonate (Ni$(acac)_2$) and Fe(III) acetylacetonate (Fe$(acac)_3$) were found to be the most suitable precursor combination, enabling the fabrication of phase-pure $Fe_xNi_{1-x}O$. In the following, the samples will be labeled as NP-X%, with X being the Fe content.

The samples with Fe contents up to 20 mol % show broadened reflections of phase-pure $Fe_xNi_{1-x}O$ in the X-ray diffraction (XRD) patterns, indicating the formation of small crystalline particles (Figure 1a). The formation of any additional Fe phases could not be observed, which indicates complete incorporation of Fe atoms into the NiO lattice. The reflections show a shift to lower 2θ angles with increasing doping concentrations, implying that the lattice constants are shifted to higher values, which indicates substitutional incorporation of Fe ions into the NiO rock salt structure. The size of the nanocrystals calculated from the line broadening in the XRD patterns decreases with higher Fe doping concentration and corresponds to 3.8 ± 0.1 nm for NP-0%, 3.0 ± 0.1 nm for NP-5%, 2.0 ± 0.1 nm for NP-10%, 1.6 ± 0.1 nm for NP-15%, and 1.5 ± 0.1 nm for NP-20%, respectively. The particle size decreases almost linearly with increasing doping concentration, as calculated for the most intensive (200) NiO reflection in the XRD patterns using the Scherrer equation

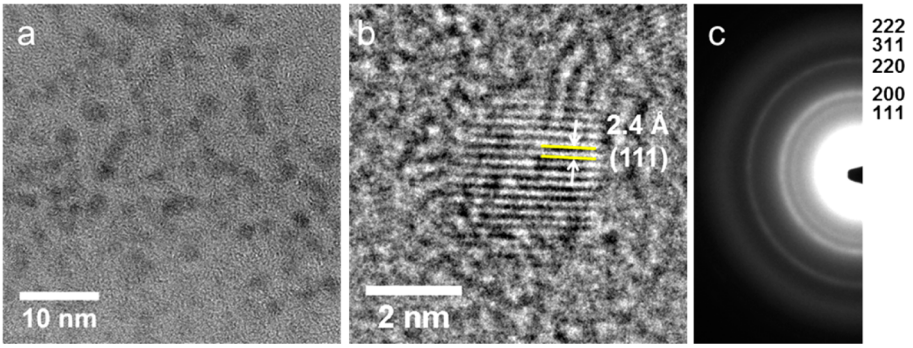

Figure 2. TEM images of the $Fe_{0.1}Ni_{0.9}O$ nanoparticles (NP-10%): (a) Overview of the nanoparticles dispersed on the TEM grid. (b) HRTEM image of a single $Fe_{0.1}Ni_{0.9}O$ nanoparticle. (c) Electron diffraction pattern taken of several tens of $Fe_{0.1}Ni_{0.9}O$ nanoparticles. The corresponding *d*-values are 2.44 Å (111), 2.09 Å (200), 1.47 Å (220), 1.26 Å (311), and 1.2 Å (222).

(Figure 1b). The lattice parameters of the $Fe_xNi_{1-x}O$ nanoparticles are in agreement with Vegard's law (Figure S1 in the Supporting Information). The particles are nonagglomerated and form stable colloidal dispersions in ethanol with the addition of very small amounts of acetic acid. As an example, ethanolic dispersions of NP-0%, NP-5%, and NP-10% with concentrations of 2 mg mL^{-1} are shown in Figure 1c.

Transmission electron microscopy (TEM) images of nanoparticles containing 10% Fe (Figure 2a,b) and 20% Fe (Figure S2 in the Supporting Information) show nonagglomerated crystals with a narrow particle size distribution (Figure S3 in the Supporting Information). The presence of lattice fringes and the absence of defects in HRTEM images (Figure 2b) reveal the single-crystalline structure of the individual particles. The electron diffraction pattern taken of an area of about 150 nm in diameter shows several rings due to averaging over several tens of particles (Figure 2c). The rings can be indexed using the NiO rock salt structure, confirming the XRD results. The average particle size determined from the TEM images is 2.0 ± 0.4 nm and 1.8 ± 0.4 nm for the particles containing 10% and 20% Fe, respectively. This is in good agreement with the sizes calculated from XRD patterns.

X-ray photoelectron spectroscopy measurements of NP-10% show the Ni 2p doublet typical for NiO in the energy region between 850 and 870 eV (Figure 3b).[36−38] The binding energies at 711 and 724 eV correspond to Fe $2p_{3/2}$ and Fe $2p_{1/2}$ peaks, respectively (Figure 3a). These signal positions are typical for Fe_2O_3 and indicate the presence of Fe atoms in the oxidation state +III.[39,40] At the same time, the presence of a separate Fe_2O_3 phase can be excluded due to missing shakeup satellites at 719 and 732 eV,[40] indicating the incorporation of Fe(III) into the NiO lattice. Quantification of the elements for NP-10% shows an atomic ratio of Ni:Fe = 12:1, corresponding to 8% Fe, which is slightly lower than the Fe(III) content of 10% in the reaction mixture and the value of 11% determined in energy-dispersive X-ray spectroscopy (EDX) measurements, and may be attributed to surface defects.

For a more detailed investigation of the oxidation state of Fe atoms within the nanoparticles, ^{57}Fe Mössbauer spectra were recorded for the samples NP-10% and NP-20%. The spectra are characterized by a paramagnetic quadrupole doublet with isomer shift values characteristic for Fe(III) ions in the high-spin state, 0.37 and 0.33 mm s^{-1} for NP-10% and NP-20%, respectively (Figure 3c, Figure S4 and Table S1 in the Supporting Information).[41] The increase in the amount of the incorporated iron caused an increase of the electric field gradient (quadrupole splitting increase from 0.49 mm s^{-1} to 0.66 mm s^{-1}), which can be attributed to a reduced symmetry of the chemical environment around the nucleus. The results reveal the presence of high-spin Fe(III) ions in octahedral sites, which is consistent with a successful incorporation of Fe(III) into the rock salt structure of NiO.[42]

X-ray absorption spectroscopy was used to examine the oxidation state and the position of Fe and Ni atoms within the $Fe_xNi_{1-x}O$ lattice. For comparison, NP-0% and NP-20% were analyzed both in powder form and after deposition on a FTO electrode. In addition, commercially available NiO powder (Sigma-Aldrich) and Fe_2O_3 (Sigma-Aldrich) were measured as references. The oxidation state of the Ni ions is +II and that of the Fe ions +III as judged from the X-ray absorption near-edge structure (XANES) spectra and by comparison of the absorption edge position with the measured references (Figure S5 in the Supporting Information). No difference in the edge shape or position was found between the nanoparticles in powder form and those deposited on the electrode. Information about the atomic structure can be obtained from the extended X-ray absorption fine structure (EXAFS) spectra. Comparing the Fourier transforms of the EXAFS spectra shown in Figure 3d, it can be seen that the local atomic structure around both Ni and Fe centers is identical to that of the rock salt structure of the NiO reference. This structure is confirmed by the simulations as shown in Figures S6, S7 and Tables S3, S4 in the Supporting Information. The different amplitudes of the peaks indicate different degrees of local

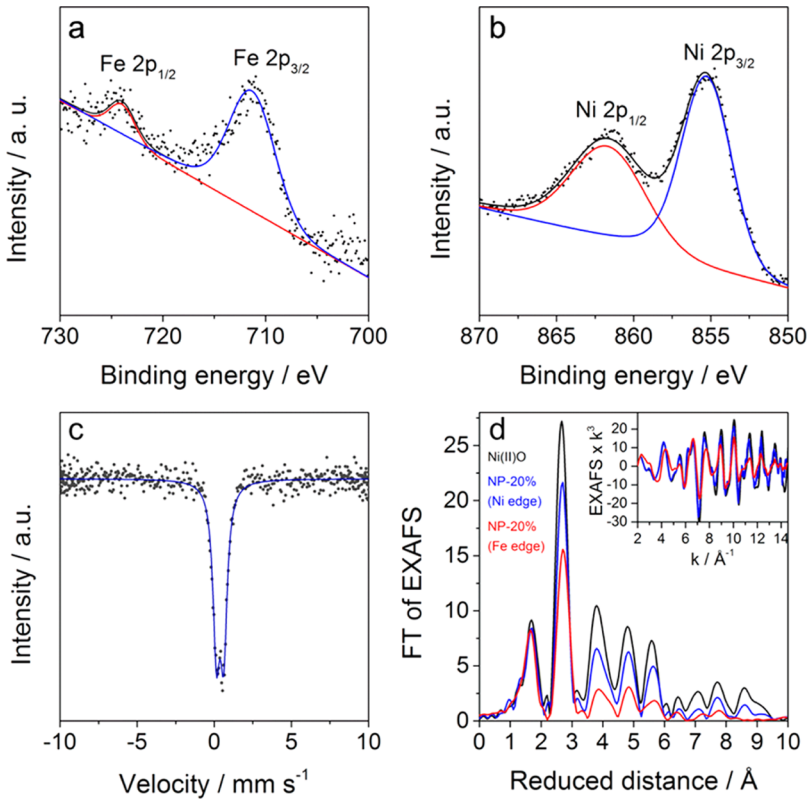

Figure 3. X-ray photoelectron spectra of 10% Fe(III)-doped NiO nanoparticles. (a) Fe 2p peaks and (b) Ni 2p peaks. Spectra were taken using a Mg source. The points correspond to the experimental spectra, and the lines are the fitted curves and the Gaussian individual peak fits, respectively. The corresponding fitting parameters are listed in Table S2 (Supporting Information). (c) Mössbauer spectrum of the sample NP-10%. (d) Fourier-transformed EXAFS spectra collected from 20% Fe(III)-doped NiO nanoparticles at the Ni (blue line) and Fe (red line) K-edges and crystalline NiO reference (black line). The original k^3-weighted spectra are shown in the inset.

disorder, which is reflected in the simulations by the higher Debye−Waller factor (lower peak amplitudes) for the nanoparticles. Another possible reason for the decrease in the peak amplitudes of the higher coordination shells in the nanoparticles is the higher proportion of surface atoms, for which not all long-range shells exist. Particularly high disorder or, alternatively, a higher proportion of surface atoms is found around the Fe centers. As evident from the EXAFS spectrum, the Fe centers in the NP-20% are located in a rock salt-type structure and thus either are incorporated into the NiO lattice or form their own Fe-only phase, which is rather unlikely since HRTEM images only show single crystalline nanoparticles. Ni and Fe ions behave virtually identically as X-ray backscatterers, and it is not possible to distinguish them in the EXAFS analyses (Figure S7 and Table S4 in the Supporting Information). However, the Fe K-edge position shows that iron is in the oxidation state +III, and the EXAFS simulations at the Fe K-edge result in Fe−O distances of 2.01 Å, matching those expected for Fe(III) in octahedral coordination and not the one for Fe(II).[43] Since the rock salt structure is not compatible with the oxidation state of +III of the Fe ions, we conclude that in the Fe-doped NiO nanoparticles individual Fe ions are incorporated in the Ni oxide lattice replacing Ni ions. A situation where Fe is predominantly on the surface of the NiO nanoparticle thus preventing the further growth of the crystals cannot be excluded and could explain the smaller particle size with Fe doping. However, in this case the Fe needs to be part of the same rock salt lattice, as evident from the virtually identical EXAFS spectra measured at the Ni and at the Fe edges.

Different studies report a limited solubility of Fe in NiO (up to 6 mol %) accompanied by the formation of a Ni−Fe spinel or Fe_2O_3 phase at low calcination temperatures.[44,45] Landon *et al.*[39] describe the formation of an additional $NiFe_2O_4$ phase with increasing Fe content in the NiO lattice already at around 5% Fe. In our material we do not observe any formation of additional phases up to at least 20 mol % Fe according to the results of several methods such as XRD, Mössbauer spectroscopy, and EXAFS, which supports the assumption that the Fe atoms are incorporated into the NiO structure. Additionally, Raman spectra of NP-0% and NP-20% showing only the presence of the $Fe_xNi_{1-x}O$ phase are shown in Figure S8 in the Supporting Information. The unusually high solubility of Fe in the rock salt NiO structure can originate from the kinetic control of the Fe-NiO phase formation in a solvothermal process, as well as the effect of the

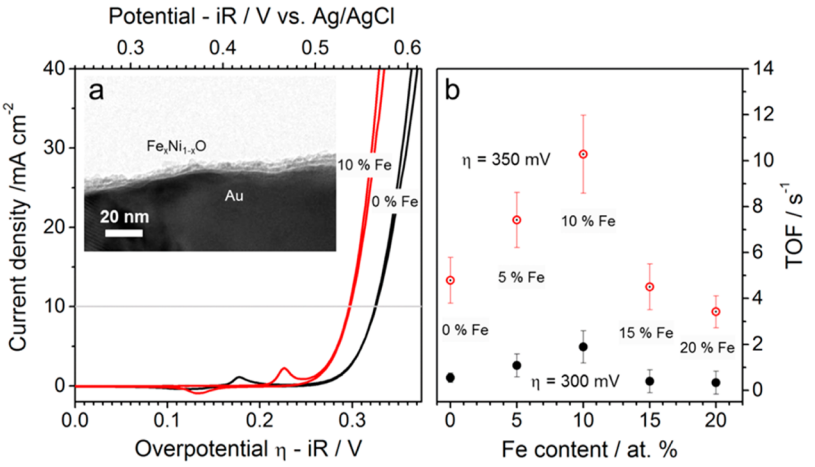

Figure 4. (a) Cyclic voltammograms of Au/QCM electrodes coated with thin films of NP-0% and NP-10%. The inset shows a cross-section HR-TEM image of the NP-10% film deposited by spin-coating on the Au/QCM substrate. (b) TOF values at an overpotential of η = 300 mV (filled circles) and η = 350 mV (open circles) for NP-0%, NP-5%, NP-10%, NP-15%, and NP-20%.

nanoscale where the metastable and defect phases often show higher stability than in the bulk.

To test the catalytic activity of Fe-doped NiO nanoparticles in electrochemical water oxidation, the particle dispersions were deposited as thin films on gold electrodes of the piezoelectric quartz crystals for the exact determination of their loading using the Sauerbrey equation.[46] Spin coating of the particle dispersions results in the formation of uniform films with an average thickness of 8 nm (Figure 4a, inset).

The voltammograms of both undoped and Fe-doped NiO thin film electrodes show reversible oxidation peaks corresponding to the reaction $Fe_xNi_{1-x}O - (1-x)e^- + (1-x)OH^- \rightleftarrows Fe_xNi_{1-x}OOH_{1-x}$, followed by the current corresponding to the OER reaction at more positive potentials. The introduction of Fe atoms into the NiO lattice leads to a positive shift in the formal potential of the first process from 389 mV *vs* Ag/AgCl for the undoped nanoparticles to 420 mV for the NP-10% particles, indicating that the electrochemical oxidation of $Ni(OH)_2$ to NiOOH is suppressed with increasing Fe content, which was also observed in previous studies.[21,22,24,29] Electrochemical measurements show that the peak area and the formal potential do not change over several hundred cycles, revealing a high stability of the Fe-doped material. A typical example of a stability measurement where the electrode potential was measured for 10 h and for 3 h at constant current densities of 10 and 200 mA cm^{-2}, respectively, is shown in Figure S9 in the Supporting Information.

According to the CV curves, the highest current densities and therefore the highest catalytic activity were obtained for 10% Fe(III)-doped NiO nanoparticles. The current densities rise with increasing doping concentration from NP-0% to NP-10% and drop significantly with further increase in Fe content, with NP-15% and NP-20% showing even lower catalytic activities than the undoped NiO sample.

In order to quantify the electrocatalytic activity of the Fe-doped NiO nanoparticles, we calculated turnover frequency values (corresponding to the moles of oxygen evolved per second per active site) at different overpotentials. This is one of the generally accepted figures of merit of electrocatalytic materials.[19−21] A critical issue in TOF calculation is the assessment of the active surface area, which is often challenging for thin electroactive layers. For our films deposited from nanoparticle dispersions on the piezoelectric Au/quartz electrodes we could determine surface areas precisely from the specific surface area of 117 $m^2 g^{-1}$ determined by nitrogen sorption (Figure S10 in the Supporting Information) and the measured mass loading of 22.5 μg cm^{-2}. Using the theoretical surface density of Ni atoms of 4.08 $\times$ 10^{14} cm^{-2} in NP-10% and the fraction of Ni atoms on the surface (X-ray photoelectron spectroscopy, XPS) we obtained a surface charge of 1.50 mC cm^{-2}. This value closely agrees with the charge obtained by integration of the voltammetric peaks of the $Fe_xNi_{1-x}O - (1-x)e^- + (1-x)OH^- \rightleftarrows Fe_xNi_{1-x}OOH_{1-x}$ process (1.43 mC cm^{-2}), corresponding to 5 $\pm$ 2% of the total Ni content, indicating that only surface atoms are involved in the electrochemical reaction.

The TOF values calculated by this method for all Fe doping concentrations at overpotentials of η = 300 mV and η = 350 mV are shown in Figure 4b. As already noticed for the current densities, the turnover frequencies increase with higher doping concentration up to 10%, showing TOF values of 0.55 s^{-1} at η = 300 mV for pure NiO (NP-0%), 1.1 s^{-1} for NP-5%, and an extremely high value of 1.9 s^{-1} for NP-10%. With a further increase in Fe content the TOF strongly decreases, showing values of only 0.39 and 0.33 s^{-1} at η = 300 mV for NP-15% and NP-20%, respectively. The TOF value obtained for the NP-10% nanoparticles not only favorably compares to other NiO-based

compounds but is one of the highest reported so far for different known types of OER materials.[7,8,13,19,32] The Tafel slope for the electrode with the best performance (NP-10%) is 37 mV dec^{-1} (Figure S11 in the Supporting Information), which is a typical value for anhydrous Fe/Ni oxides.[22]

The high OER electrocatalytic activity of ultrasmall nickel oxide nanoparticles was already reported by us previously.[32] The beneficial effect of the reduced crystal size of undoped NiO to only a few nanometers and the surface properties of the nanoparticles on the catalytic performance is shown by the very high TOF values (0.55 s^{-1}) compared to bulk material. When doping the nanocrystals with iron, the catalytic activity of the NiO is even further increased with TOF values of up to 1.9 s^{-1} for NP-10% in the present study.

It should be noted that the TOF values reported for different materials strongly depend on the method of surface area determination. McCrory *et al.*[20] and Louie *et al.*[21] presented a route for the calculation of the surface area using the measured capacitance of the material. Following this method, we have obtained a surface area of 0.35 cm^2 using the measured capacitance of 21 μF (Figure S12 in the Supporting Information) and assuming a specific capacitance of 60 μF cm^{-2} for flat oxide electrodes,[47] which is almost 10 times lower than the specific surface area determined by the direct method described above. The use of this surface area leads to a greatly overestimated TOF value of 17 s^{-1} for NP-10%, which is almost 10 times higher than the TOF obtained by the direct method. The large discrepancy between the TOF values determined with different methods suggests that the results obtained from the capacitance measurements should be interpreted with great care and only be used for the estimation of activity trends in the same type of materials, but not for the calculation of absolute values. The error in the surface area determination should become even more significant for insulating or poorly conducting layers, such as $Fe_{1-x}Ni_xO$, where an increase in surface area does not necessarily translate into an increase in the double-layer capacitance. A similar point was raised by Louie *et al.*,[21] who obtained drastically different TOF values for the same materials using a different calculation method. Thus, they calculated extremely high TOF values of up to 87 s^{-1} (TOF_{max}) from capacitive measurements assuming that only surface Ni atoms are catalytically active and very small values of 0.005–0.008 s^{-1} (TOF_{min}) for the same material assuming that each atom in the layer is electrocatalytically active. The application of the latter method of TOF determination to our system (taking the amount of the Ni atoms from the mass loading) leads to a TOF_{min} value of 0.26 s^{-1}, which is 30 times higher than the TOF_{min} reported by Louie *et al.* However, similar to the results of Louie *et al.*, this value is much lower than the TOF_{max} of 17 s^{-1} calculated for the same NP-10% film, which again shows that this method should be applied with great care.

McCrory *et al.*[20] recently described a method to benchmark OER catalysts. For example, they calculated the current density for a given overpotential of 350 mV. The two materials with the best catalytic performance were IrO_x (42 mA cm^{-2}) and $NiFeO_x$ (15 mA cm^{-2}). Following this method, we obtained a current density of 59 ± 5 mA cm^{-2} at an overpotential of 350 mV for the electrode with 10% Fe-doped NiO. This value is higher than that of any other reported OER known to us including other $NiFeO_x$ morphologies.[7,8,13,19,30] This demonstrates the strong impact of morphology and nanoscaling on the electrocatalytic performance, which opens new perspectives for the further development of active electrocatalysts.

To conclude, higher Fe(III) doping concentrations increased the catalytic activity of Fe-doped NiO NPs. A similar observation is described in the literature for mixed iron nickel oxide phases. These mixed metal oxide catalysts attained the best OER activity for 10% Fe(III) content.[39] The same applies to solution-cast thin films with the formal composition $Fe_xNi_{1-x}O$.[19]

In addition to the extremely high electrocatalytic activity, the excellent dispersibility of the $Fe_xNi_{1-x}O$ nanoparticles offers additional advantages, such as a great flexibility towards the fabrication of different electrode architectures. Thus, thin homogeneous layers can be obtained by spin coating of particle dispersions. It is also expected that the nanoparticles can be homogeneously distributed on porous substrates with complex geometry by drop casting.

CONCLUSION

We describe a novel synthesis route for the preparation of ultrasmall, crystalline, and dispersible NiO nanoparticles substitutionally doped with Fe(III). They reveal great potential as an extremely efficient, inexpensive catalyst for the electrochemical oxygen evolution. Various undoped and Fe-doped NiO nanoparticles were successfully synthesized using a solvothermal reaction in *t*BuOH with the acetylacetonates of nickel(II) and iron(III) serving as precursors. In this way, ultrasmall and highly dispersible nanocrystals of doped nickel oxide with Fe doping concentrations of up to 20% could be obtained. The particles form stable, non-agglomerated, colloidal dispersions in ethanol. The particle size is in the range of 1.5–3.8 nm and strongly depends on the doping concentration, leading to smaller particles with increasing iron content. The presence of iron as Fe(III) and nickel as Ni(II) on the surface and within the nanoparticles was confirmed by XPS, EXAFS, and Mössbauer spectroscopy. The electrocatalytic activity of NiO is clearly enhanced with increasing Fe doping concentration, reaching an optimum at 10% iron content. The highest turnover frequency of 1.9 s^{-1} was obtained for Fe(III)-doped NiO nanoparticles even at a

low overpotential of 300 mV, outperforming expensive catalysts such as iridium oxide. The unique features of these Fe-doped NiO nanocrystals provide great potential for their application as an efficient and competitive anode material in the field of electrochemical water splitting.

EXPERIMENTAL SECTION

Synthesis of $Fe_xNi_{1-x}O$ Nanoparticles. Nickel(II) acetylacetonate was purchased from Alfa Aesar (95% purity), iron(III) acetylacetonate was purchased from Sigma-Aldrich (97% purity), and *tert*-butanol was purchased from Sigma-Aldrich (puriss. p.a., ACS reagent, ≥99.7%). All chemicals were used as received except for *tert*-butanol, which was dried over a 4 Å molecular sieve at 28 °C and filtered prior to use.

For the solvothermal synthesis of iron-doped nickel oxide nanoparticles 917.5 mg (3.571 mmol) of nickel(II) acetylacetonate ($Ni(acac)_2$) was mixed with iron(III) acetylacetonate ($Fe(acac)_3$) in the desired molar composition. The Fe doping concentration, $c_{doping,Fe}$, was calculated using the equation $c_{doping,Fe} = n_{Fe}/(n_{Ni} + n_{Fe})$ with n_x being the molar amount of the respective precursor. For 5%, 10%, 15%, and 20% Fe doping 66.4 mg (0.188 mmol), 140.5 mg (0.397 mmol), 164.9 mg (0.466 mmol), and 210.6 mg (0.595 mmol) of the iron precursor was added, respectively. The solid mixture was mixed with 100 mL of *tert*-butanol under vigorous stirring in a glass autoclave liner, forming an orange suspension, then placed into a Parr Series 4760 pressure vessel (300 mL) autoclave reactor and hermetically sealed. The reactions were carried out under continuous stirring at 205 °C for 20 h in the case of 5% and 10% doping and for 30 h in the case of 15% and 20% doping, resulting in uniform brown dispersions of nanoparticles. The as-prepared particles were dried in air by evaporating the solvent at 80 °C on a hot plate. At these conditions phase pure iron-doped nickel oxide nanoparticles with 3.8 ± 0.1 nm (0% Fe), 3.0 ± 0.1 nm (5% Fe), 2.0 ± 0.1 nm (10% Fe), 1.6 ± 0.1 nm (15% Fe), and 1.5 ± 0.1 nm (20% Fe) in size were obtained.

Dispersions of the Fe-doped and undoped NiO nanoparticles were prepared in ethanol by the addition of acetic acid. In a typical procedure, 1.1 mg of the dried powder was covered with 8 μL of acetic acid. After sonication for 5 min the particles were dispersed in 500 μL of ethanol (absolute) and sonicated for another 5 min to obtain a colloidal dispersion with a metal oxide concentration of 0.03 mol L^{-1}.

Characterization of $Fe_xNi_{1-x}O$ Nanoparticles. Wide-angle X-ray diffraction analysis was carried out in transmission mode using a STOE STADI P diffractometer with $CuK_{\alpha 1}$-radiation (λ = 1.540 60 Å) and a Ge(111) single-crystal monochromator equipped with a DECTRIS MYTHEN 1K solid-state strip detector. Powder XRD patterns of the samples were collected with an omega-2-theta scan in a 2θ range from 5° to 70° with a step size of 1°, a fixed counting time of 90 s per step, and a resolution of 0.05°. The size of the crystalline domains was calculated from the XRD patterns for the most intensive (200) reflection using the Scherrer equation.

TEM measurements were carried out using a FEI Titan 80-300 instrument equipped with a field emission gun operated at 300 kV. For the sample preparation a drop of a strongly diluted dispersion of a sample in ethanol was deposited on a holey carbon-coated copper grid and evaporated. Contaminations were removed by hydrogen-oxygen plasma cleaning for 15 s at 50 mW and large-area illumination in the TEM for 40 min. The cross sections were prepared following a procedure described by Strecker *et al.*[48]

X-ray photoelectron spectroscopy analysis of the particles was performed on a silicon substrate using a VSW HA 100 electron analyzer, and the K_α radiation was provided by a non-monochromatized magnesium anode system (Mg K_α = 1253.6 eV). Ar ion polishing was done at 1000 eV for 10 min. The recorded elemental peaks were fitted using a Doniach–Sunjic function,[49] and the elemental ratios were calculated by the equation

$$\frac{X_A}{X_B} = \frac{I_A/S_A}{I_B/S_B}$$

where I_A/I_B is the ratio of fitted areas and S is the sensitivity factor.

^{57}Fe Mössbauer spectra were recorded at 20 °C in the transmission mode using a standard WissEl (Starnberg, Germany) instrumental configuration. A ^{57}Co/Rh Mössbauer source was used. The velocity scale and all data refer to the metallic α-Fe absorber at 20 °C. A quantitative analysis of the recorded spectra was made using the MossWinn program.

X-ray absorption spectra (XANES/EXAFS) were collected at the BESSY synchrotron radiation source operated by the Helmholtz-Zentrum Berlin. The measurements were acquired at the KMC-1 bending-magnet beamline at 20 K in a cryostat (Oxford-Danfysik) with a liquid-helium flow system. The powder samples were diluted by mixing with boron nitride (BN) powder (Sigma-Aldrich) to a ratio of 1:10 and measured in absorption mode using ionization chambers (Oxford-Danfysik). The films deposited on FTO were measured in fluorescence mode using a 13-element energy-resolving Ge detector (Canberra) and selecting the Ni or Fe Kα fluorescence emission. The data were collected up to 800 eV above the Ni and Fe absorption K-edges. After the ionization chamber used to measure the absorption of the sample, Ni or Fe metal foil was placed and measured in absorption mode as internal energy standard. The energy calibration was done by shifting the energy axis such that the first inflection point in the absorption edge of the Fe foil corresponds to 7112 eV and for the Ni foil to 8333 eV. These values were used as E_0 in the conversion of the energy axis from eV to k scale when extracting the EXAFS spectrum. For the Fourier transformation a cosine window function was applied on 10% from both sides of the EXAFS range between k = 2.3 and 14.4 $Å^{-1}$. Further details related to data evaluation and error calculation are given in previous studies.[50]

Nitrogen sorption measurements were carried out at 77 K with dried powders of $Fe_xNi_{1-x}O$ nanoparticles using a Quantachrome Autosorb iQ instrument. The powders were degassed at 150 °C for at least 12 h before measurement.

Raman spectroscopy was carried out using a LabRAM HR UV–vis (Horiba Jobin Yvon) Raman microscope (Olympus BX41) with a Symphony CCD detection system and a He–Ne laser (λ = 633 nm). Spectra were recorded using a lens with a 50-fold magnification.

Electrochemical Measurements. The electrodes were prepared by deposition of the dispersed iron-doped nickel oxide nanoparticles by spin coating on quartz crystal microbalance (QCM) crystals (KVG 10 MHz QCM devices with gold electrodes from Quartz Crystal Technology GmbH). For the spin-coating method 8 μL of nickel oxide dispersion was deposited on a masked QCM crystal exposing an area of 0.196 cm^2 and spun at 1000 rpm for 10 s. The QCM electrodes prepared in this way were subsequently heated to 240 °C in a laboratory oven with a heating ramp of 4 °C min^{-1} and a dwell time of 2 h, resulting in ~8 nm thick films.

The mass loading was calculated from the resonance frequencies of the QCM crystals before and after coating using the Sauerbrey equation $\Delta f = -C_f \times \Delta m$ with Δf being the change in frequency, C_f the sensitivity factor of the QCM crystal, and Δm the change in mass.[46]

Electrochemical measurements were performed in a three-electrode setup using an Autolab PGSTAT302N potentiostat/galvanostat with an FRA32 M module operating with Nova 1.10.2 software. All measurements were performed in 0.5 M KOH electrolyte solution (Sigma-Aldrich, volumetric solution) at pH 13.43. Pt mesh (2 cm^2) was used as a counter electrode. Au/QCM crystals coated with $Fe_xNi_{1-x}O$ nanoparticles were used as working electrodes. To provide an electrical connection to the QCM electrode, a silver wire was connected to the respective part of the QCM crystal using silver lacquer.

The silver lacquer and the wire were sealed afterward in inert two-component epoxy resin (Gatan, Inc.). All potentials were measured *vs* a Ag/AgCl/KCl (sat.) reference electrode with a potential of +0.989 V *vs* the reversible hydrogen electrode at pH 13.43 (+0.197 V *vs* NHE). The electrochemical data were corrected for uncompensated resistance, R_s. R_s was determined as minimum total impedance in the frequency regime between 10 and 50 kHz at open circuit conditions and at a potential of 0.2 V *vs* Ag/AgCl, where no faradaic processes take place. Ninety-five percent of the measured resistance was compensated. R_s was typically around 6−8 ohm for all $Fe_xNi_{1-x}O$-coated Au/QCM electrodes. The overpotential η was calculated using the equation $\eta = E - E_{OER} - iR_s$, where E is the potential recorded *vs* the Ag/AgCl reference electrode, E_{OER} is the reversible potential of the OER *vs* the Ag/AgCl reference electrode (0.240 V at pH 13.43), and i is the current. Current densities are calculated using the geometric surface area of the Au/QCM electrode (0.196 cm^2).

The preconditioning of the NiO electrodes was performed using cyclic voltammetry (CVA). The electrodes were cycled between 0 and 0.7 V *vs* Ag/AgCl in 0.5 M KOH at a scan rate of 20 mV s^{-1} until the current had reached stable values and did not change anymore with repetitive cycling at scan rates of 20 mV s^{-1} (typically 35 cycles).

The turnover frequency at an overpotential of $\eta = 0.3$ V was calculated on the basis of active Ni atoms according to TOF = $i/(4Q_{exp})$, where i is the current and Q_{exp} is the charge corresponding to the Fe-NiO redox reaction according to the equation $Fe_xNi_{1-x}O - (1 - x)e^- + (1 - x)OH^- \rightleftarrows Fe_xNi_{1-x}OOH_{1-x}$ assuming that only one electron is transferred per Ni atom. As the charge obtained from the anodic peak of the NiO redox process may contain some contribution from the OER process, we have used the cathodic peak to determine the amount of the catalytically active Ni atoms.

The ratio of catalytically active sites to the theoretical total number of active sites was calculated using the relation of the experimental charge values Q_{exp} to the theoretical charge values Q_{th} (Q_{exp}/Q_{th}). Q_{exp} was obtained by integration of the cathodic peak, which corresponds to the reduction of NiOOH to NiO. Q_{th} was calculated using the total amount of $Fe_xNi_{1-x}O$ in the films. For NP-0% to NP-20% the ratio Q_{exp}/Q_{th} is between 3% and 9%, indicating that only surface atoms are catalytically active.

The surface area was determined from N_2-sorption isotherms (BET surface area) and calculated *via* measurements of the electrochemical capacitance of the interface between the film and the electrolyte. In this method the electrodes were cycled potentiostatically in a potential range where no oxidation or reduction processes take place, typically between 0.17 and 0.23 V *vs* Ag/AgCl/KCl (sat.) at scan rates ranging from 1 to 20 mV s^{-1}. The measured capacitance was obtained by plotting the capacitance current at 0.2 V against the scan rate (Figure S12 in the Supporting Information).

The stability of the Fe-doped NiO electrodes was tested using the 10% doped sample. The electrode potential was measured at a constant current density of 10 mA cm^{-2} for 10 h and at 200 mA cm^{-2} for 3 h *vs* Hg/HgO/1 M KOH in 0.5 M KOH.

Conflict of Interest: The authors declare no competing financial interest.

Supporting Information Available: TEM images, particle size distribution, Mössbauer spectra, XANES and EXAFS spectra with simulation parameters of $Fe_{0.2}Ni_{0.8}O$ nanoparticles, and electrochemical characterization of electrodes assembled from nanoparticles including Tafel analysis and stability tests. This material is available free of charge *via* the Internet at http://pubs.acs.org.

Acknowledgment. The authors are grateful to the German Research Foundation (DFG, grant no. FA 839/3-1 and SPP 1613), the NIM cluster (DFG), the research networks "Solar Technologies Go Hybrid" and UMWELTnanoTECH (State of Bavaria), the Center for NanoScience (CeNS), and the DAAD for financial support.

REFERENCES AND NOTES

1. Cook, T. R.; Dogutan, D. K.; Reece, S. Y.; Surendranath, Y.; Teets, T. S.; Nocera, D. G. Solar Energy Supply and Storage for the Legacy and Nonlegacy Worlds. *Chem. Rev.* **2010**, *110*, 6474–6502.
2. Walter, M. G.; Warren, E. L.; McKone, J. R.; Boettcher, S. W.; Mi, Q.; Santori, E. A.; Lewis, N. S. Solar Water Splitting Cells. *Chem. Rev.* **2010**, *110*, 6446–6473.
3. Nørskov, J. K.; Bligaard, T.; Logadottir, A.; Kitchin, J. R.; Chen, J. G.; Pandelov, S.; Stimming, U. Trends in the Exchange Current for Hydrogen Evolution. *J. Electrochem. Soc.* **2005**, *152*, J23–J26.
4. Dau, H.; Limberg, C.; Reier, T.; Risch, M.; Roggan, S.; Strasser, P. The Mechanism of Water Oxidation: From Electrolysis *via* Homogeneous to Biological Catalysis. *ChemCatChem* **2010**, *2*, 724–761.
5. Bockris, J. O. M. Kinetics of Activation Controlled Consecutive Electrochemical Reactions: Anodic Evolution of Oxygen. *J. Chem. Phys.* **1956**, *24*, 817–827.
6. Zhao, Z.; Wu, H.; He, H.; Xu, X.; Jin, Y. A High-Performance Binary Ni-Co Hydroxide-Based Water Oxidation Electrode with Three-Dimensional Coaxial Nanotube Array Structure. *Adv. Funct. Mater.* **2014**, *24*, 4698–4705.
7. Yeo, B. S.; Bell, A. T. In Situ Raman Study of Nickel Oxide and Gold-Supported Nickel Oxide Catalysts for the Electrochemical Evolution of Oxygen. *J. Phys. Chem. C* **2012**, *116*, 8394–8400.
8. Liu, X.; Wang, F. Transition Metal Complexes that Catalyze Oxygen Formation from Water: 1979−2010. *Coord. Chem. Rev.* **2012**, *256*, 1115–1136.
9. Dincă, M.; Surendranath, Y.; Nocera, D. G. Nickel-Borate Oxygen-Evolving Catalyst that Functions under Benign Conditions. *Proc. Natl. Acad. Sci. U.S.A.* **2010**, *107*, 10337–10341.
10. Suntivich, J.; May, K. J.; Gasteiger, H. A.; Goodenough, J. B.; Shao-Horn, Y. A Perovskite Oxide Optimized for Oxygen Evolution Catalysis from Molecular Orbital Principles. *Science* **2011**, *334*, 1383–1385.
11. Kim, T. W.; Choi, K. S. Nanoporous $BiVO_4$ Photoanodes with Dual-Layer Oxygen Evolution Catalysts for Solar Water Splitting. *Science* **2014**, *343*, 990–994.
12. Reier, T.; Oezaslan, M.; Strasser, P. Electrocatalytic Oxygen Evolution Reaction (OER) on Ru, Ir, and Pt Catalysts: A Comparative Study of Nanoparticles and Bulk Materials. *ACS Catal.* **2012**, *2*, 1765–1772.
13. Trotochaud, L.; Boettcher, S. W. Precise Oxygen Evolution Catalysts: Status and Opportunities. *Scr. Mater.* **2014**, *74*, 25–32.
14. Chen, Z.; Meyer, T. J. Copper(II) Catalysis of Water Oxidation. *Angew. Chem., Int. Ed.* **2013**, *52*, 700–703.
15. Grimaud, A.; Carlton, C. E.; Risch, M.; Hong, W. T.; May, K. J.; Shao-Horn, Y. Oxygen Evolution Activity and Stability of $Ba_6Mn_5O_{16}$, $Sr_4Mn_2CoO_9$, and $Sr_6Co_5O_{15}$: The Influence of Transition Metal Coordination. *J. Phys. Chem. C* **2013**, *117*, 25926–25932.
16. Trasatti, S. Electrocatalysis by Oxides − Attempt at a Unifying Approach. *J. Electroanal. Chem. Interfacial Electrochem.* **1980**, *111*, 125–131.
17. Matsumoto, Y.; Sato, E. Electrocatalytic Properties of Transition Metal Oxides for Oxygen Evolution Reaction. *Mater. Chem. Phys.* **1986**, *14*, 397–426.
18. Man, I. C.; Su, H.-Y.; Calle-Vallejo, F.; Hansen, H. A.; Martínez, J. I.; Inoglu, N. G.; Kitchin, J.; Jaramillo, T. F.; Nørskov, J. K.; Rossmeisl, J. Universality in Oxygen Evolution Electrocatalysis on Oxide Surfaces. *ChemCatChem* **2011**, *3*, 1159–1165.
19. Trotochaud, L.; Ranney, J. K.; Williams, K. N.; Boettcher, S. W. Solution-Cast Metal Oxide Thin Film Electrocatalysts for Oxygen Evolution. *J. Am. Chem. Soc.* **2012**, *134*, 17253–17261.
20. McCrory, C. C. L.; Jung, S.; Peters, J. C.; Jaramillo, T. F. Benchmarking Heterogeneous Electrocatalysts for the Oxygen Evolution Reaction. *J. Am. Chem. Soc.* **2013**, *135*, 16977–16987.
21. Louie, M. W.; Bell, A. T. An Investigation of Thin-Film Ni−Fe Oxide Catalysts for the Electrochemical Evolution of Oxygen. *J. Am. Chem. Soc.* **2013**, *135*, 12329–12337.

22. Corrigan, D. A. The Catalysis of the Oxygen Evolution Reaction by Iron Impurities in Thin Film Nickel Oxide Electrodes. *J. Electrochem. Soc.* **1987**, *134*, 377–384.
23. Corrigan, D. A. Effect of Coprecipitated Metal Ions on the Electrochemistry of Nickel Hydroxide Thin Films: Cyclic Voltammetry in 1M KOH. *J. Electrochem. Soc.* **1989**, *136*, 723–728.
24. Hu, C.-C.; Wu, Y.-R. Bipolar Performance of the Electroplated Iron−Nickel Deposits for Water Electrolysis. *Mater. Chem. Phys.* **2003**, *82*, 588–596.
25. Miller, E. L.; Rochelaeu, R. E. Electrochemical Behavior of Reactively Sputtered Iron-Doped Nickel Oxide. *J. Electrochem. Soc.* **1997**, *144*, 3072–3077.
26. Chen, Y.-W. D.; Noufi, R. N. Electrodeposition of Nickel and Cobalt Oxides onto Platinum and Graphite Electrodes for Alkaline Water Electrolysis. *J. Electrochem. Soc.* **1984**, *131*, 731–735.
27. Gong, M.; Li, Y.; Wang, H.; Liang, Y.; Wu, J. Z.; Zhou, J.; Wang, J.; Regier, T.; Wei, F.; Dai, H. An Advanced Ni-Fe Layered Double Hydroxide Electrocatalyst for Water Oxidation. *J. Am. Chem. Soc.* **2013**, *135*, 8452–8455.
28. Trotochaud, L.; Young, S. L.; Ranney, J. K.; Boettcher, S. W. Nickel-Iron Oxyhydroxide Oxygen-Evolution Electrocatalysts: The Role of Intentional and Incidental Iron Incorporation. *J. Am. Chem. Soc.* **2014**, *136*, 6744–6753.
29. Li, X.; Walsh, F. C.; Pletcher, D. Nickel Based Electrocatalysts for Oxygen Evolution in High Current Density, Alkaline Water Electrolysers. *Phys. Chem. Chem. Phys.* **2011**, *13*, 1162–1167.
30. Smith, R. D.; Prevot, M. S.; Fagan, R. D.; Trudel, S.; Berlinguette, C. P. Water Oxidation Catalysis: Electrocatalytic Response to Metal Stoichiometry in Amorphous Metal Oxide Films Containing Iron, Cobalt, and Nickel. *J. Am. Chem. Soc.* **2013**, *135*, 11580–11586.
31. Smith, R. D.; Prevot, M. S.; Fagan, R. D.; Zhang, Z.; Sedach, P. A.; Siu, M. K.; Trudel, S.; Berlinguette, C. P. Photochemical Route for Accessing Amorphous Metal Oxide Materials for Water Oxidation Catalysis. *Science* **2013**, *340*, 60–63.
32. Fominykh, K.; Feckl, J. M.; Sicklinger, J.; Döblinger, M.; Böcklein, S.; Ziegler, J.; Peter, L.; Rathousky, J.; Scheidt, E.-W.; Bein, T.; Fattakhova-Rohlfing, D. Ultrasmall Dispersible Crystalline Nickel Oxide Nanoparticles as High-Performance Catalysts for Electrochemical Water Splitting. *Adv. Funct. Mater.* **2014**, *24*, 3123–3129.
33. Szeifert, J. M.; Feckl, J. M.; Fattakhova-Rohlfing, D.; Liu, Y.; Kalousek, V.; Rathousky, J.; Bein, T. Ultrasmall Titania Nanocrystals and Their Direct Assembly into Mesoporous Structures Showing Fast Lithium Insertion. *J. Am. Chem. Soc.* **2010**, *132*, 12605–12611.
34. Liu, Y.; Szeifert, J. M.; Feckl, J. M.; Mandlmeier, B.; Rathousky, J.; Hayden, O.; Fattakhova-Rohlfing, D.; Bein, T. Niobium-Doped Titania Nanoparticles: Synthesis and Assembly into Mesoporous Films and Electrical Conductivity. *ACS Nano* **2010**, *4*, 5373–5381.
35. Feckl, J. M.; Fominykh, K.; Doblinger, M.; Fattakhova-Rohlfing, D.; Bein, T. Nanoscale Porous Framework of Lithium Titanate for Ultrafast Lithium Insertion. *Angew. Chem., Int. Ed.* **2012**, *51*, 7459–7463.
36. Biesinger, M. C.; Payne, B. P.; Grosvenor, A. P.; Lau, L. W. M.; Gerson, A. R.; Smart, R. S. C. Resolving Surface Chemical States in XPS Analysis of First Row Transition Metals, Oxides and Hydroxides: Cr, Mn, Fe, Co and Ni. *Appl. Surf. Sci.* **2011**, *257*, 2717–2730.
37. Hoffer, B.; Dickvanlangeveld, A.; Janssens, J.; Bonne, R.; Lok, C.; Moulijn, J. Stability of Highly Dispersed Ni/AlO Catalysts: Effects of Pretreatment. *J. Catal.* **2000**, *192*, 432–440.
38. McIntyre, N. S.; Cook, M. G. X-Ray Photoelectron Studies on Some Oxides and Hydroxides of Cobalt, Nickel, and Copper. *Anal. Chem.* **1975**, *47*, 2208–2213.
39. Landon, J.; Demeter, E.; İnoğlu, N.; Keturakis, C.; Wachs, I. E.; Vasić, R.; Frenkel, A. I.; Kitchin, J. R. Spectroscopic Characterization of Mixed Fe−Ni Oxide Electrocatalysts for the Oxygen Evolution Reaction in Alkaline Electrolytes. *ACS Catal.* **2012**, *2*, 1793–1801.
40. Yamashita, T.; Hayes, P. Analysis of XPS Spectra of Fe^{2+} And Fe^{3+} Ions in Oxide Materials. *Appl. Surf. Sci.* **2008**, *254*, 2441–2449.
41. Douvalis, A. P.; Jankovic, L.; Bakas, T. The Origin of Ferromagnetism in ^{57}Fe-Doped NiO. *J. Phys.: Condens. Matter* **2007**, *19*, 436203–436228.
42. Horner, O.; Mouesca, J.-M.; Oddou, J.-L.; Jeandey, C.; Niviere, V.; Mattioli, T. A.; Mathe, C.; Fontecave, M.; Maldivi, P.; Bonville, P.; *et al*. Mössbauer Characterization of an Unusual High-Spin Side-On Peroxo-Fe^{3+} Species in the Active Site of Superoxide Reductase from *Desulfoarculus baarsii*. Density Functional Calculations on Related Models. *Biochemistry* **2004**, *43*, 8815–8825.
43. Kanowitz, S. M.; Palenik, G. J. Bond Valence Sums in Coordination Chemistry Using Oxidation-State-Independent R_0 Values. A Simple Method for Calculating the Oxidation State of Iron in Fe-O Complexes. *Inorg. Chem.* **1998**, *37*, 2086–2088.
44. Raghavan, V. Fe-Ni-O (Iron-Nickel-Oxygen). *J. Phase Equilib. Diffus.* **2010**, *31*, 369–371.
45. Wulf, G. L.; Carter, T. J.; Wallwork, G. R. The Oxidation of FeNi Alloys. *Corros. Sci.* **1969**, *9*, 689–701.
46. Sauerbrey, G. Verwendung von Schwingquarzen zur Wägung Dünner Schichten und zur Mikrowägung. *Z. Phys. A: Hadrons Nucl.* **1959**, *155*, 206–222.
47. Trasatti, S.; Petrii, O. A. Real Surface Area Measurements in Electrochemistry. *Pure Appl. Chem.* **1991**, *63*, 711–734.
48. Strecker, A.; Salzberger, U.; Mayer, J. Specimen Preparation for Transmission Electron Microscopy: Reliable Methods for Cross-Sections and Brittle Materials. *Prakt. Metallogr.* **1993**, *30*, 482–487.
49. Doniach, S.; Sunjic, M. Many-Electron Singularity in X-Ray Photoemission and X-Ray Line Spectra from Metals. *J. Phys. C: Solid State Phys.* **1970**, *3*, 285–291.
50. Wiechen, M.; Zaharieva, I.; Dau, H.; Kurz, P. Layered Manganese Oxides for Water-Oxidation: Alkaline Earth Cations Influence Catalytic Activity in a Photosystem II-Like Fashion. *Chem. Sci.* **2012**, *3*, 2330–2339.